



Dual decomposition pathways for L-aspartic acid on Ni(100)

Michael Radetic^a, Andrew J. Gellman^{a,b,*}

^a Department of Chemical Engineering, Carnegie Mellon University, 5000 Forbes Ave., Pittsburgh, PA 15213, United States

^b W.E. Scott Institute for Energy Innovation, Carnegie Mellon University, 5000 Forbes Ave., Pittsburgh, PA 15213, United States

ARTICLE INFO

Keywords:

Aspartic acid
Decomposition
Reaction kinetics
Mechanism
Surface chemistry
Isotopomers

ABSTRACT

The thermal decomposition of aspartic acid (Asp, HO₂CCH(NH₂)CH₂CO₂H) on Ni surfaces occurs by a more complex pathway than on Cu surfaces where it decomposes via an aspartate species to yield CO₂, H₂, and CH₃C≡N stoichiometrically. In addition to these three products observed on Cu, the decomposition mechanism on Ni yields CO, H₂O and HC≡N. Herein, we probe the Asp decomposition mechanism on Ni(100) by X-ray photoelectron spectroscopy and by temperature programmed reaction spectra of a variety of adsorbed aspartic acid isotopomers (L-Asp, 1-¹³C-L-Asp, 4-¹³C-L-Asp, 1,4-¹³C₂-L-Asp, 3,4-¹³C₂-L-Asp, 1,2,3,4-¹³C₄-¹⁵N-L-Asp, ¹⁵N-L-Asp, and D₇-L-Asp). These isotope labeling experiments provide insight into the regiospecific origin within adsorbed aspartic acid of the carbon and nitrogen atoms found in the desorbing products. At low coverage, the adsorbed aspartic acid primarily undergoes inter- and intra-molecular condensation/dehydration to ketone and/or anhydride intermediates that ultimately yield CO. At higher coverages, the decomposition process is similar to that observed on Cu surfaces yielding mostly CO₂ from the terminal carboxyl groups and CH₃C≡N from the interior of the adsorbed aspartic acid. The continued presence of CO and H₂O products at high coverages suggests the persistence of the condensation/dehydration reactions across all coverages.

1. Introduction

The stereospecific binding of chiral pharmaceuticals with human enzymes necessitates the design of highly enantioselective catalysts or separation processes for the production of enantiomerically pure drugs. Indeed, numerous examples highlight the dramatically different physiological impacts that result from ingestion of the two enantiomers of a chiral compound [1–3]. Heterogeneous catalysis can serve as a means for the production of enantiomerically pure compounds, if the catalyst has a chiral atomic structure and is enantiomerically pure. In the context of chiral heterogeneous catalysts, the structure of the catalyst is of fundamental importance for achieving enantioselectivity. The structure must lack mirror symmetry at the surface to create a stereochemical environment that favors the formation of one enantiomer over the other [4].

One common method of rendering a chiral surface is through the adsorption of a chiral molecule onto an achiral surface, thus breaking the surface symmetry. The natural abundance of chiral biological molecules such as amino acids as well as their significance in pharmaceutical applications makes them ideal candidates for use as chiral surface modifiers. There are many studies examining the fundamental surface

chemistry of chiral modifiers and their utility in catalytic reactions [5–10]. In addition to enantioselective catalysis, chiral surfaces can induce enantiomer purification via adsorption [11–13] due to enantio-specific differences in enantiomer adsorption energies on chiral surfaces. One of the well-studied examples of enantioselective catalysis with high product enantiomeric excess is the enantioselective hydrogenation of β-ketoesters using a surface modified with pure enantiomers of tartaric acid (TA) [10,14]. Adsorption of such chiral modifiers can alter the adsorption geometry of prochiral molecules as a result of enantiospecific interactions between the chiral modifier and prochiral reagent [15–18]. In certain systems, adsorption of a chiral molecule may induce surface reconstruction into a chiral structure, a process known as chiral imprinting [19–22].

Understanding the molecule-surface interactions and reaction mechanisms of chiral adsorbates is critical for describing enantioselective catalytic processes and discovering new chiral modifiers. Amino acids are among the most highly studied classes of chiral adsorbates [23]. The bonding configurations, decomposition mechanisms, and reaction kinetics proposed for amino acids adsorbed on metallic surfaces depend on the substrate metal [24–28] and its crystallographic orientation [9,24,27,29]. On Cu surfaces, we have observed that aspartic acid

* Corresponding author.

E-mail address: gellman@cmu.edu (A.J. Gellman).

<https://doi.org/10.1016/j.susc.2021.121980>

Received 26 June 2021; Received in revised form 3 October 2021; Accepted 27 October 2021

Available online 31 October 2021

0039-6028/© 2021 Elsevier B.V. All rights reserved.

(Asp, $\text{HO}_2\text{CCH}(\text{NH}_2)\text{CH}_2\text{CO}_2\text{H}$) bonds as doubly deprotonated aspartate ($\text{Cu-O}_2\text{CCH}(\text{NH}_2)\text{CH}_2\text{CO}_2\text{-Cu}$) at 400 K and decomposes via an autocatalytic surface explosion mechanism [28,30,31]. The use of ^{13}C isotope labeled L-Asp revealed the sequence of decomposition steps during temperature programmed reaction spectroscopy (TPRS) [28]. Cleavage of the 3C-4C bond yields the first CO_2 , followed by cleavage of the 1C-2C bond to yield a second CO_2 and finally dehydrogenation of the remaining $\text{C}_2\text{H}_5\text{N}$ species to yield acetonitrile ($\text{CH}_3\text{C}\equiv\text{N}$). Deuterium labeling revealed scrambling of H(D) during the formation of $\text{CH}_3\text{C}\equiv\text{N}$ [30]. On Ni(111), Wilson et al. [29] also observed that Asp decomposition at high coverage yields H_2 and CO_2 products suggesting that Asp bonds anionically as aspartate to the Ni(111) surface. However, at low coverages, the presence of imide ($-\text{C}(=\text{O})\text{NHC}(=\text{O})-$) bands in the reflection absorption infrared spectra and CO production during TPRS suggest the formation of oligosuccinimide clusters via condensation/dehydration reactions. The possible existence of this decomposition pathway is consistent with the known polycondensation of aspartic acid monomers to form polysuccinimide [32,33]. Infrared absorption spectra of Asp on Pd(111) also suggests oligomerization to form polysuccinimide [26]. Through a combined experimental and computational study Quevedo et al. [27] claimed that the primary bonding mode of Asp on Ni(100) is a pentadentate configuration at both low and high coverages. In contrast to the study by Wilson et al. on Ni(111) [29], Quevedo et al. [27] suggest that anionic aspartate on Ni(100) produces CO_2 during heating and that oligosuccinimide formation does not occur. The differences between these two studies on Ni(111) and Ni(100) presumably arises from the different crystallographic orientations of the surfaces. Such structure sensitivity has also been suggested to be the origin of differences in the surface chemistry of tartaric acid on Ni(111) [24] and Ni(110) [9]. In contrast, the crystallographic orientation of Cu surfaces alters the decomposition kinetics slightly, but does not significantly influence the decomposition pathway or product distributions of TA and Asp decomposition [30,31,34].

This study aims to understand and describe the mechanism of L-Asp decomposition on Ni(100). X-ray photoemission spectroscopy (XPS) has been used to identify the chemical state of Asp on Ni(100). This work builds on prior work principally by using a set of eight ^{13}C and ^{15}N isotopomers of L-Asp (L-Asp, $1-^{13}\text{C}$ -L-Asp, $4-^{13}\text{C}$ -L-Asp, $1,4-^{13}\text{C}_2$ -L-Asp, $3,4-^{13}\text{C}_2$ -L-Asp, $1,2,3,4-^{13}\text{C}_4-^{15}\text{N}$ -L-Asp, ^{15}N -L-Asp, and D_7 -L-Asp) to determine the regiospecific origins of C and N atoms found in the desorbing decomposition products of Asp/Ni(100). XPS reveals that two co-adsorbed Asp states, anionic and zwitterionic, appear at coverages in the range 0.15 to 2.7 ML. The low coverage decomposition products consist of CO, CO_2 , H_2 , and H_2O . At higher coverages, $\text{CH}_3\text{C}\equiv\text{N}$ and $\text{HC}\equiv\text{N}$ products emerge. Further investigation using isotopic labeling supports the presence of two primary decomposition pathways. At low Asp coverages, where scanning tunneling microscopy (STM) images on Ni(111) and Pd(111) reveal adsorption at step edges [24,26], the primary decomposition pathway includes condensation/dehydration to generate intermediates such as oligosuccinimide and polyaspartate. During thermal decomposition these yield significant amounts of CO. At higher coverage on Ni(100), the adsorbed species is predominantly aspartate which decomposes to yield CO_2 , H_2 , and $\text{CH}_3\text{C}\equiv\text{N}$.

2. Experiment

2.1. X-ray photoemission spectroscopy (XPS)

XPS was conducted in a ThermoFisher ThetaProbe™ capable of operating at a pressure of 1×10^{-9} Torr. The Ni(100) single-crystal, purchased from Monocrystals Corp., has a diameter of 10 mm and thickness of 2 mm and was brazed to a Cu block that was mounted to a heatable sample holder. A chromel-alumel (K-type) thermocouple was spot welded to the edge of the Ni(100) crystal. The Ni(100) sample can be heated to $T > 1000$ K via thermal contact with a resistive BN heating element and it can be cooled using liquid nitrogen to $T < 250$ K.

The Ni(100) sample surface was cleaned by Ar^+ sputtering at 1 kV followed by annealing to $T = 1000$ K. The surface cleanliness was verified by XPS spectra obtained at five points across the Ni(100) surface. Physical vapor deposition of Asp onto the Ni(100) surface was performed with a homemade sublimation evaporator operating at 438 K in a sample preparation chamber connected to the analysis chamber of the ThetaProbe™. During exposure to Asp vapor, the Ni(100) sample was held at 250 K.

All XPS spectra were collected with the Ni(100) sample at 300 K. XPS spectra were obtained at three different coverages: submonolayer, monolayer, and multilayer. To achieve the submonolayer coverage, the sample was maintained at 250 K, the doser was held at 438 K, and the dosing time was 5 min. After exposure to Asp, the sample was transferred to the analysis chamber of the ThetaProbe for XPS. For the multilayer exposure, the sample (250 K) and doser (438 K) temperatures were used with a 2 h dosing time. After collecting the multilayer XPS spectrum, the sample was heated at 2 K/s to 405 K to remove the multilayer and then immediately quenched, leaving a monolayer on the surface. During XPS data collection, the sample was held at room temperature (300 K) using an X-ray spot size of 400 μm , a pass energy of 200 eV, and an energy step size of 0.1 eV.

2.2. Temperature programmed reaction spectroscopy (TPRS)

All TPRS experiments were conducted in a stainless steel ultrahigh-vacuum (UHV) chamber capable of operating at pressures below 1×10^{-9} Torr. The chamber was equipped with a $xyz-\theta$ sample manipulator allowing independent translation and rotation of the Ni(100) crystal within the chamber. The Ni(100) crystal was mounted by spot welding Ta wires connected to the manipulator to opposite edges of the crystal. A chromel-alumel (K-type) thermocouple was also spot welded to the edge of the crystal. A minimum temperature of 90 K was attainable with the use of liquid nitrogen and the sample could be heated resistively to > 1100 K. An Ar^+ sputter ion gun was used to clean the surface of the Ni(100) crystal and low-energy electron diffraction (LEED) allowed verification of the crystal lattice of the cleaned surface. Physical deposition of Asp onto the Ni(100) surface was performed using a two-cell Kentax® sublimation evaporator. A Hiden® quadrupole mass spectrometer identified Asp decomposition products and measured their rates of desorption from the Ni(100) surface during heating.

Upon cleaning the Ni(100) surface, the desired Asp isotopomer was heated in the doser to a temperature in the range 435–438 K and the Ni(100) was placed 6 cm from the sublimation source. The sample temperature was maintained at 250 K during all Asp exposures. Depending on the desired coverage, the dosing temperatures and times were 3 min with a doser temperature of 435 K for low coverage studies, 30 min exposure times with a doser temperature of 438 K for monolayer formation, or 2 h exposure times with a doser temperature of 438 K for multilayer formation. After dosing at the desired temperature for the appropriate time, the sample was moved to a position ~ 2 mm from the aperture to the mass spectrometer and heated at a constant rate of 2 K/s with the mass spectrometer continuously monitoring signals at specified m/z ratios to obtain a TPRS spectrum. Initial experiments obtained low temperature resolution TPRS at all m/z ratios in the range 1–100 amu. Subsequent investigations were restricted to those m/z ratios that yielded significant TPRS signals.

The following chemicals were introduced into the UHV chamber used for TPRS via a leak valve to either calibrate the mass spectrometer signal versus partial pressure or to identify the compound's fragmentation pattern: acetonitrile ($\text{CH}_3\text{C}\equiv\text{N}$, Thermo-Fisher 99.9% purity), carbon monoxide (CO, Matheson, 99.5% purity), and carbon dioxide (CO_2 , Matheson, 99.5% purity).

Powdered L-Asp samples ($\geq 98\%$ atomic purity) and $3,4-^{13}\text{C}_2$ -L-Asp (99% atomic purity) were purchased from Sigma-Aldrich. All remaining used isotopomers of Asp have an atomic purity of 99% unless stated otherwise and were purchased from Cambridge Isotope Laboratories.

The eight Asp isotopomers used in this study were: L-Asp, $1-^{13}\text{C}$ -L-Asp, $4-^{13}\text{C}$ -L-Asp, $1,4-^{13}\text{C}_2$ -L-Asp, $3,4-^{13}\text{C}_2$ -L-Asp, $1,2,3,4-^{13}\text{C}_4-^{15}\text{N}$ -L-Asp, ^{15}N -L-Asp and D_7 -L-Asp (98% atomic purity).

3. Results

3.1. Chemical state of L-Asp/Ni(100)

In order to identify the chemical state of L-Asp on the Ni(100) surface, XPS spectra of the C1s, N1s, and O1s core levels (Fig. 1) were collected at three different coverages determined on the basis of XPS intensities relative to those of the monolayer: submonolayer ($\theta \cong 0.3$),

monolayer ($\theta = 1.0$), and multilayer ($\theta = 2.7$). The XPS spectra were taken with the Ni(100) surface at 300 K while all L-Asp exposures were conducted with the surface at $T = 250$ K. Unconstrained Gaussian peak fitting to the XPS spectra was performed using the curve fit function in SciPy to reveal the chemical states of the atoms present on the surface and to quantify their relative amounts.

The L-Asp multilayer was deposited onto the clean Ni(100) surface at 250 K by dosing L-Asp for 2 h. At multilayer thick films, most amino acids tend to adopt a zwitterionic state ($^-\text{O}_2\text{CCH}(\text{NH}_3^+)\text{CH}_2\text{CO}_2\text{H}$) [27, 28,30,35,36]. On the Cu(110) and Cu(100) surfaces, adsorbed Asp multilayers form the zwitterionic species and their XPS spectra exhibit four C1s peaks with core level binding energies centered at 285.8 eV for

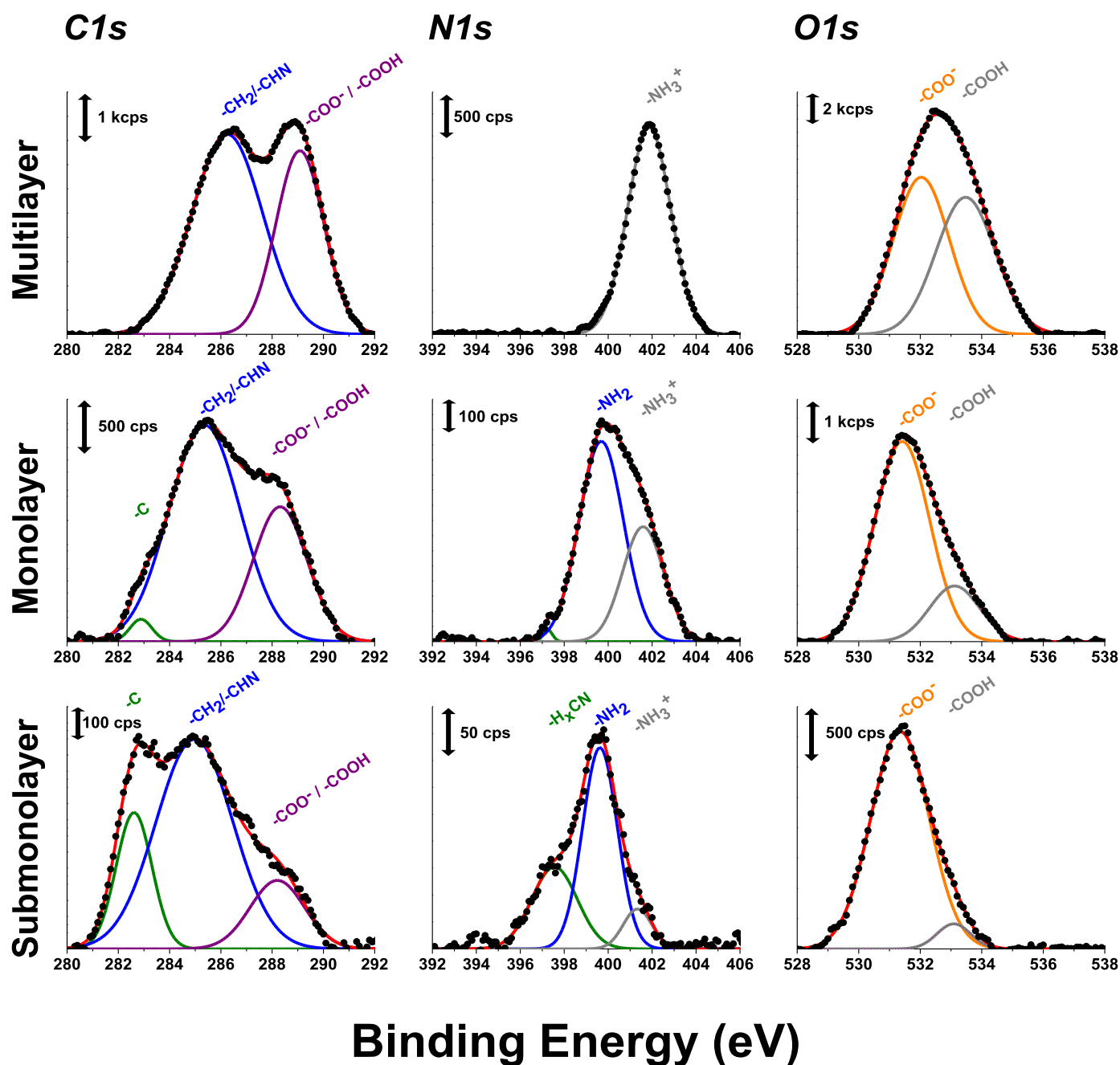


Fig. 1. XPS spectra of the C1s, N1s, and O1s levels of L-Asp on Ni(100) at three different coverages: multilayer ($\theta = 2.7$ ML, top row), monolayer ($\theta = 1$ ML, middle row), and submonolayer ($\theta = 0.3$ ML, bottom row). Multilayer: The presence of NH_3^+ in the N1s spectrum and equal amounts of COO^- and COOH in the O1s spectrum reveals L-Asp adsorbed as a zwitterion. Monolayer: These same features (NH_3^+ , COO^- , COOH) appear in the monolayer although the NH_2 and COO^- peaks indicate the predominance of the anionic aspartate configuration. Submonolayer: The peaks associated with aspartate are most intense at submonolayer coverages. Additional decomposition fragments such as H_xCN and carbidic C appear at low coverage as well as some small zwitterionic features (NH_3^+ , COOH).

CH₂, 286.9 eV for CH(NH₃⁺), 288.6 eV for COO⁻ and 289.5 eV for COOH [27,28,30]. Because molecules in the multilayer are not interacting directly with the surface, their core level binding energies on different metal surfaces should be comparable. The C1s multilayer spectrum from L-Asp on Ni(100) was fitted using two peaks centered at 286.2 eV (CH₂ and CHN) and 289.1 eV (COO⁻/COOH). These binding energies match the mean values of those reported for these C atoms in L-Asp on Cu(110).

Evidence for the zwitterionic state is given by the N1s spectrum, which exhibits a single peak at 401.9 eV, corresponding to NH₃⁺. This closely matches the N1s binding energy of 402.2 eV measured on Cu(110) [28] and those reported on other surfaces [36,37]. The O1s peaks from COO⁻ and COOH in L-Asp on Ni(100) exhibit binding energies of 532.0 eV and 533.5 eV, respectively, and match well with the values of 532.0 and 533.2 eV reported on Cu(110) [28]. Finally, the ratio of the O1s peak areas for the COO⁻ and COOH groups is ~1:1 indicating the presence of equal amounts of the COO⁻ and COOH groups, as expected for the zwitterion.

The L-Asp monolayer on Ni(100) was created by heating the multilayer at 2 K/s to 405 K (above the multilayer desorption temperature of 390 K) and then quenching to 300 K. Fig. 1 reveals the presence of zwitterionic N1s and O1s peaks arising from the NH₃⁺ (401.6 eV) and COOH (533.1 eV) groups. However, the dominant peak in the N1s spectrum has a binding energy of 399.7 eV and arises from NH₂. Furthermore, the ratio of the O1s peak areas for COO⁻ (531.4 eV) and COOH (533.1 eV), is ~4 suggesting that at a coverage of one monolayer, L-Asp on Ni(100) is present predominantly, but not exclusively, in its doubly-deprotonated, aspartate form, Ni-O₂CCH(NH₂)CH₂CO₂-Ni. On the Cu(110) and Cu(100) surfaces [28,30], monolayer Asp is also known to bind as aspartate. Quevedo [27] suggested on the basis of DFT calculations and XPS spectra that Asp/Ni(100) forms a pentadentate structure with the four oxygen atoms from both carboxylate groups and the NH₂ group all bonded directly to the Ni surface. While this may be the optimal structure in the absence of molecular interactions, the presence of the NH₃⁺ and COOH in the monolayer suggests the presence of co-adsorbed zwitterionic Asp and doubly deprotonated aspartate. XPS spectra of alanine on Ni(111) [36] and Asp on Ni(100) [27] also support the co-existence of anionic and zwitterionic alanine states. In Fig. 1, the primary C1s peaks found in the monolayer XPS spectrum include the CH₂/CHN peaks at 285.4 eV and the COO⁻/COOH groups located at 288.3 eV. The presence of the COOH peak in the O1s spectrum of the L-Asp monolayer indicates that the COO⁻ peak in the monolayer C1s spectrum contains some contribution from COOH that is not resolved from the primary COO⁻ peak. Similarly, the C1s binding energies attributed to CH(NH₃⁺) and CH(NH₂) have slightly different binding energies (286.9 eV and 286.0 eV) on Cu(110) [28] and are not resolved in the broad C1s peak attributed to the CH₂ and CHN groups. In addition to the reduction in intensity of the NH₃⁺ N1s and COOH O1s peaks at monolayer coverage with respect to those at multilayer coverage, the C1s peak for CH₂/CH(NH₂) shifts from 286.2 to 285.4 eV and the C1s peak for COO⁻/COOH shifts from 289.1 to 288.3 eV. This shift supports the suggestion that less zwitterionic Asp is present in the monolayer than in the multilayer and that the zwitterionic Asp coexists with an anionic aspartate state. Lastly, some carbide surface carbon also appears with a peak position located at 282.9 eV, as found in [27].

The creation of the L-Asp submonolayer on Ni(100) required a 5 min exposure of the Ni(100) surface to L-Asp. For the C1s L-Asp spectrum, the peaks arise from carbide carbon at 282.6 eV, the CH₂/CH(N) groups at 285.0 eV, and the COO⁻ peak at 288.2 eV. In the N1s spectrum, the peaks include a H_xCN decomposition product at 397.6 eV as suggested by [27], NH₂ at 399.6 eV, and NH₃⁺ at 401.3 eV. Lastly, the O1s spectrum consists of the COO⁻ peak at 531.3 eV and a very small COOH peak at 533.1 eV. Again, the small amount of NH₃⁺ and COOH present in the submonolayer implies that the C1s feature labeled CH₂/CHN consists of both CH(NH₃⁺) and CH(NH₂) components while the C1s feature labeled COO⁻/COOH contains a small fraction of COOH. The H_xCN peak located

at 397.6 in the N1s spectrum is observed for both Asp [27] and alanine [36] on Ni surfaces and is claimed to arise from a molecular dissociation product. In transitioning from the monolayer to the submonolayer, the peaks attributed to anionic species (NH₂ and COO⁻) decrease in intensity, as do the peaks attributed to the zwitterionic species (NH₃⁺ and COOH). Increasing the Asp coverage above the monolayer, causes only the zwitterionic features to continue growing eventually screening some of the features such as the NH₂ peak that are attributable to the aspartate species. Hence, these findings support the presence of two distinct co-adsorbed states of L-Asp on the Ni(100) surface; these are anionic aspartate and zwitterionic conformations.

3.2. Products and kinetics of L-Asp decomposition on Ni(100)

3.2.1. Thermal decomposition of low coverage L-Asp/Ni(100)

To conduct studies of L-Asp decomposition on Ni(100) at low coverage, the surface held at 250 K was exposed for 3 min to L-Asp isotopomers emanating from the Asp doser at a temperature of 438 K. These studies were conducted in the TPRS chamber. After adsorption of L-Asp at low coverage ($\theta \cong 0.15$ based on CO₂ TPRS data, see below) on Ni(100), the sample was heated at 2 K/s in front of a mass spectrometer to collect a TPRS spectrum. Product identification was accomplished by considering the products of Asp decomposition on other surfaces [26,28,29,31] and validating the species fragmentation patterns (see SI Section 1, Fig. S1). The primary products observed desorbing from the Ni(100) surface were CO, CO₂, H₂, H₂O, CH₃C≡N, and HC≡N. The CO₂ peak area at submonolayer coverage was compared to the CO₂ TPRS peak area at monolayer coverage, $\theta = 1$, to estimate the submonolayer coverage at $\theta \cong 0.15$.

We focus first on the desorption of CO and CO₂ arising from the decomposition of L-Asp/Ni(100) at low coverage. The dashed black curves shown in Fig. 2 are the ¹²CO and ¹²CO₂ low coverage TPRS spectra during decomposition of unlabeled L-Asp. The mass spectrum signal at $m/z = 44$ was used in conjunction with the measured fragmentation pattern of CO₂ to estimate the signal at $m/z = 28$ attributable to CO desorption (i.e. the signal not arising from fragmentation of CO₂). Two peaks appear in the CO spectra with the more intense lower temperature peak centered at $T_p = 414$ K and the less intense high temperature peak at $T_p = 600$ K. In contrast, a single CO₂ feature appears at $T_p = 427$ K.

The use of isotopically labeled L-Asp provides the opportunity to isolate and establish the regiochemical origins of the decomposition products. The 600 K CO desorption peak has been attributed to associative desorption of atomic carbon and oxygen in studies on Ni foil [38] and has also been observed during Asp decomposition on Ni(111) [29]. The CO desorbing from the surface at $T_p = 600$ K in Fig. 2 arises solely from the 2-C and 3-C carbon atoms of L-Asp. The ¹³C atoms in the 1-C and 4-C positions never appear in the 600 K desorption feature (Fig. 2a solid red and dashed orange curves). This is corroborated by two additional experiments using 1,4-¹³C₂-L-Asp, and 3,4-¹³C₂-L-Asp (Fig. 3). The amount of ¹²CO desorbing at 600 K during L-Asp decomposition (Figs. 2a and 3, dashed black curve) is equivalent to the ¹²CO desorbing from 1,4-¹³C₂-L-Asp (Fig. 3 solid green line). The absence of ¹³CO in the 600 K peak of 1,4-¹³C₂-L-Asp decomposition (Fig. 3 solid red line) confirms that only the interior 2-C and 3-C of L-Asp contribute to this 600 K desorption feature. Finally, the amounts of ¹²CO (Fig. 3 solid blue line) and ¹³CO (Fig. 3 solid orange line) observed desorbing at 600 K during TPRS of 3,4-¹³C₂-L-Asp are roughly equivalent (0.56:0.46), suggesting that both interior carbons contribute equally to the 600 K desorption feature.

The 600 K CO TPRS peak arises from recombination of atomic C and O on the Ni(100) surfaces [29,38]. It is clear from Figs. 2 and 3 that only the terminal 1-C and 4-C carbon atoms contribute to the CO₂ peaks, it is also clear from Fig. 2a (solid red and dashed orange curves) that they are also contributing to the low temperature CO desorption feature at $T_p = 414$ K. This implies that there is some reaction pathway leading to

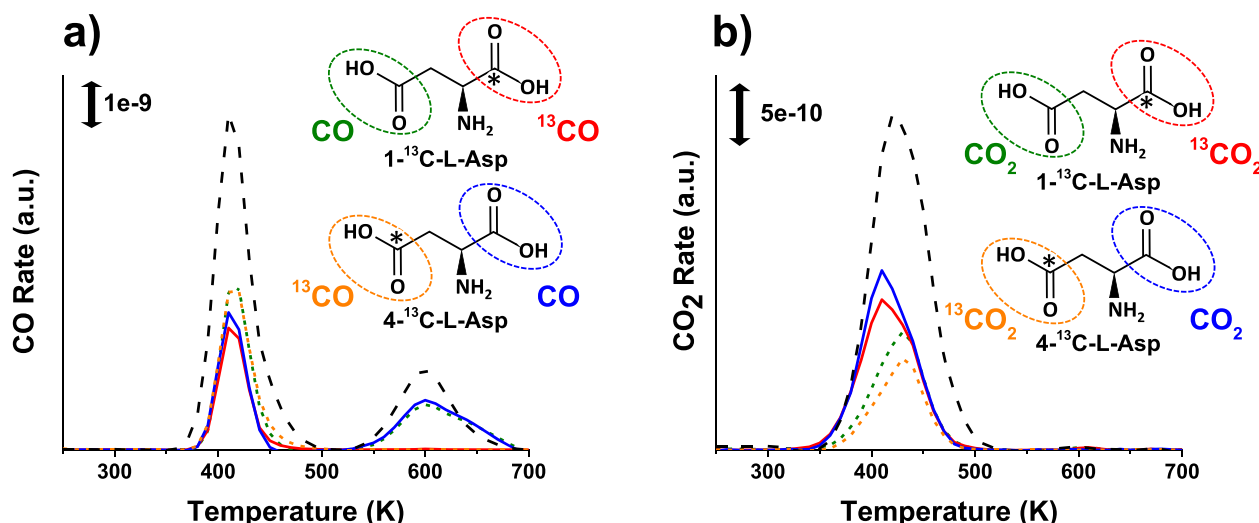


Fig. 2. TPRS spectra of low coverage ($\theta \cong 0.15$ ML) L-Asp, $1\text{-}^{13}\text{C}$ -L-Asp, and $4\text{-}^{13}\text{C}$ -L-Asp showing desorption of a) CO and b) CO_2 isotopomers. The dashed, black curves correspond to ^{12}CO and $^{12}\text{CO}_2$ arising from the decomposition of unlabeled L-Asp. The solid, red curves arise from ^{13}CO and $^{13}\text{CO}_2$ originating from the 1-C of $1\text{-}^{13}\text{C}$ -L-Asp. The dashed, green curves arise from ^{12}CO and $^{12}\text{CO}_2$ originating from the 2-, 3-, or 4-C atoms of $1\text{-}^{13}\text{C}$ -L-Asp. The solid blue curves arise from ^{12}CO and $^{12}\text{CO}_2$ originating from the 1-, 2-, or 3-C atoms of $4\text{-}^{13}\text{C}$ -L-Asp. Finally, the dashed, orange curves arise from ^{13}CO and $^{13}\text{CO}_2$ originating from the 4-C atom of $4\text{-}^{13}\text{C}$ -L-Asp.

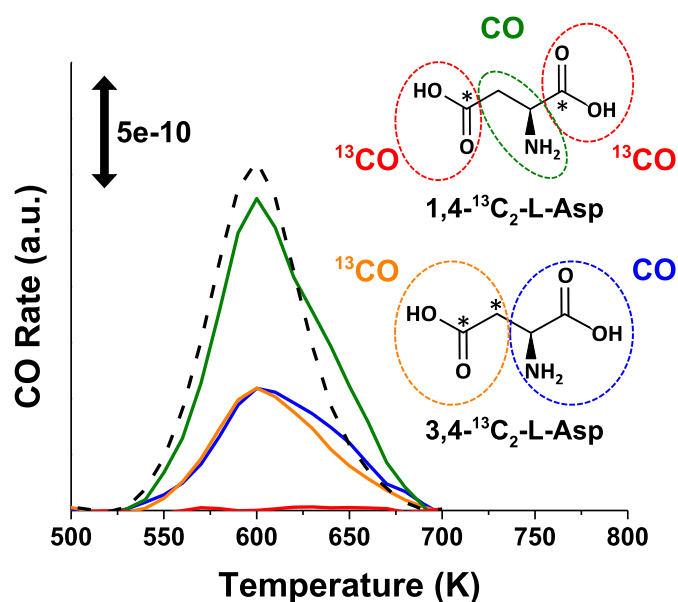


Fig. 3. Relative amount of ^{12}CO and ^{13}CO contributing to the high temperature CO desorption at 600 K for three different L-Asp isotopomers: L-Asp, $1,4\text{-}^{13}\text{C}_2$ -L-Asp, and $3,4\text{-}^{13}\text{C}_2$ -L-Asp. The observations suggest that the interior (2-C and 3-C) carbon atoms recombine with oxygen to produce this high temperature recombinative CO desorption peak.

decomposition of a fraction of the L-Asp carboxyl groups to ultimately yield CO desorption and, presumably, deposition of oxygen atoms onto the Ni(100) surface.

The use of isotope labeling reveals details of the L-Asp decomposition mechanism in the sense of which bonds break first. The solid red and blue curves in Fig. 2b reveal that the 1C-2C bond breaks first. The CO_2 originating from the 1-C atom (solid red and blue curves) desorbs at $T_p = 410$ K while the CO_2 originating from the 4-C atom via cleavage of the 3C-4C bond (dashed orange and green curves) desorbs at $T_p = 430$ K. Note that this is the opposite order to that on Cu surfaces [28,30] where the 3C-4C cleaves first and the 1C-2C cleaves second.

Lastly, for CO and CO_2 desorption, isotopic labeling reveals an asymmetry to the reaction yields. The CO yield from the 1-C carboxyl

group (Fig. 2a solid red and blue curves) is clearly lower than the yield of CO originating in the 4-C carboxyl group (dashed orange and green curves). In contrast, the selectivity towards CO_2 is opposite. The yield of 1- CO_2 (Fig. 2b, solid red and blue curves) is greater than the yield of 4- CO_2 (Fig. 2b dashed orange and green curves). While the asymmetry in desorption temperatures can arise from simple kinetic differences arising from the asymmetry of the molecule, the differences in yield must arise from some form of mechanistic selectivity.

Several hydrogen containing products were observed desorbing from the surface during TPRS of L-Asp on Ni(100): H_2 , H_2O , $\text{HC}\equiv\text{N}$ and $\text{N}\equiv\text{CCH}_3$. We focus here on H_2 and H_2O . One of the issues in studies such as this one is discrimination between the hydrogen adsorbing from the background of the UHV chamber and the hydrogen originating from the adsorbate under study. Fortunately, use of a fully deuterated L-Asp isotopomer (D_7 -L-Asp) can unambiguously differentiate between hydrogen originating from the background and that originating from the molecular adsorbate. Fig. 4a depicts the TPRS spectra of $\text{H}_2/\text{HD}/\text{D}_2$ from the Ni(100) surface following adsorption of D_7 -L-Asp at a low coverage of 0.15 ML. Desorption peaks are observed at $T_p = 344$, 405 and 451 K. The desorption of H_2 at 344 K arises from H atom recombination on the surfaces [39]. The observation of HD and D_2 also desorbing from the Ni(100) surface at 344 K suggests that during adsorption and subsequent heating of D_7 -L-Asp there has been some de-deuteration of the $-\text{CO}_2\text{D}$ groups to deposit D atoms on the surface. This is consistent with the XPS indication that an aspartate species is formed during Asp adsorption. The higher temperature TPRS peaks at $T_p = 405$ and 451 K reveal both HD and D_2 desorption, but no H_2 desorption. The presence of H atoms at these higher temperatures suggest that there has been some H-D exchange between the surface and the $-\text{ND}_2$ group or with some fraction of the $-\text{CO}_2\text{D}$ groups that are not ionic.

The water desorption peaks shown in Fig. 4b occur at $T_p = 409$ K and $T_p = 454$ K, very close to the high temperature hydrogen peaks. The observation of water desorption suggests some type of dehydration reaction that was not observed on Cu surfaces. The fact that the yield of H_2O is greater than that of D_2O suggests that there has been significant DH exchange into the Asp carboxyl groups that must be participating in the dehydration process.

3.2.2. Thermal decomposition of monolayer L-Asp/Ni(100)

L-Asp monolayers on Ni(100) at 250 K were prepared by exposure to

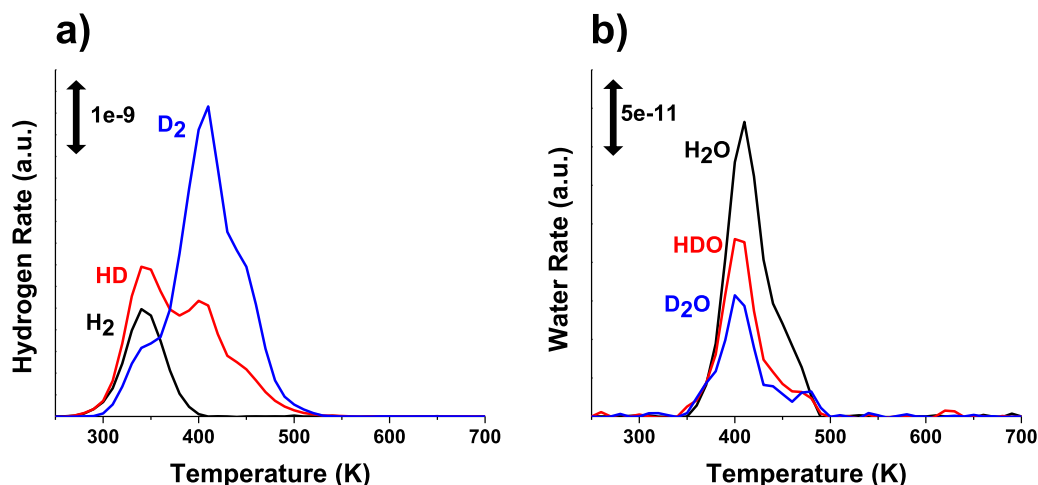


Fig. 4. TPRS spectra of hydrogen containing low coverage desorption products a) H₂, HD, D₂ and b) H₂O, HDO, D₂O from D₇-L-Asp decomposition on Ni(100). Three peaks appear in the hydrogen spectra. The T_p = 344 K peak arises from associative desorption of surface H and D atoms. The peaks at T_p = 405 K and 451 K are rate limited by Asp dehydrogenation steps. In the water spectra, a large peak occurs near T_p = 409 K and a smaller shoulder appears around T_p = 454 K. These arise from condensation/dehydration reactions in the adsorbed Asp.

fluxes of L-Asp isotopomers for 30 min using a doser temperature of 438 K. Afterwards, a TPRS spectrum was collected by heating the Ni(100) sample at 2 K/s in front of the mass spectrometer. Exposure of the Ni(100) surface to L-Asp fluxes for > 30 min resulted in the appearance of a peak at T_p = 390 K in the m/z = 2, 28, 44 TPRS spectra, consistent with the onset of Asp multilayer formation and desorption [30]. L-Asp exposure to form a monolayer on Ni(100) introduces several changes in the TPRS spectra with respect to those obtained at low coverage. These include a shifting of peak temperatures, emergence of new desorption features, and modified product yields.

The dashed black curves in Fig. 5 are the ¹²CO and ¹²CO₂ TPRS spectra obtained during the decomposition of unlabeled L-Asp at monolayer coverage. The first thing to note relative to the low coverage spectra (Fig. 2a, dashed black curve) is the absence of the CO TPRS peak at 600 K that arises from recombination of atomic C and O on the Ni(100) surface. At low coverage, there are reaction paths that lead to fragmentation of adsorbed Asp to the point that atomic O and C are deposited onto the Ni(100) surface. These pathways disappear at monolayer L-Asp coverage.

The CO TPRS spectra at monolayer L-Asp coverage as shown in

Fig. 5a reveal three features: a low temperature shoulder at T_p = 426 K, the primary peak at 469 K and a high temperature shoulder at 510 K. The low temperature feature may be associated with the low temperature peak observed at 414 K in the low coverage spectrum (Fig. 2a) but is significantly reduced in intensity in the monolayer spectrum. It might appear that the shoulder at 510 K corresponds to the low coverage CO peak at T_p = 600 K that is assigned to the recombination of atomic C and O on the surface. However, the use of isotopically labeled 1-¹³C-L-Asp (Fig. 5a, solid red curve) and 4-¹³C-L-Asp (Fig. 5a, dashed orange curve) reveals contributions of ¹³CO to the 510 K shoulder in the monolayer L-Asp TPRS, confirming that the carbon atoms in the 510 K shoulder originate in the terminal carboxyl groups (1-C and 4-C). Furthermore, summing the ¹³CO peaks produced from 1-¹³C-L-Asp and 4-¹³C-L-Asp (Fig. 5, solid red and dashed orange curves) reproduces the black ¹²CO of unlabeled L-Asp as it should, if all three CO peaks originate from the terminal carboxyl groups.

The CO₂ TPRS spectra (Fig. 5b, dashed black curve) from L-Asp decomposition at monolayer coverage on Ni(100) are quite different from those observed at low coverage (Fig. 2b, dashed black curve). Not surprisingly, the yield of CO₂ is significantly increased at monolayer

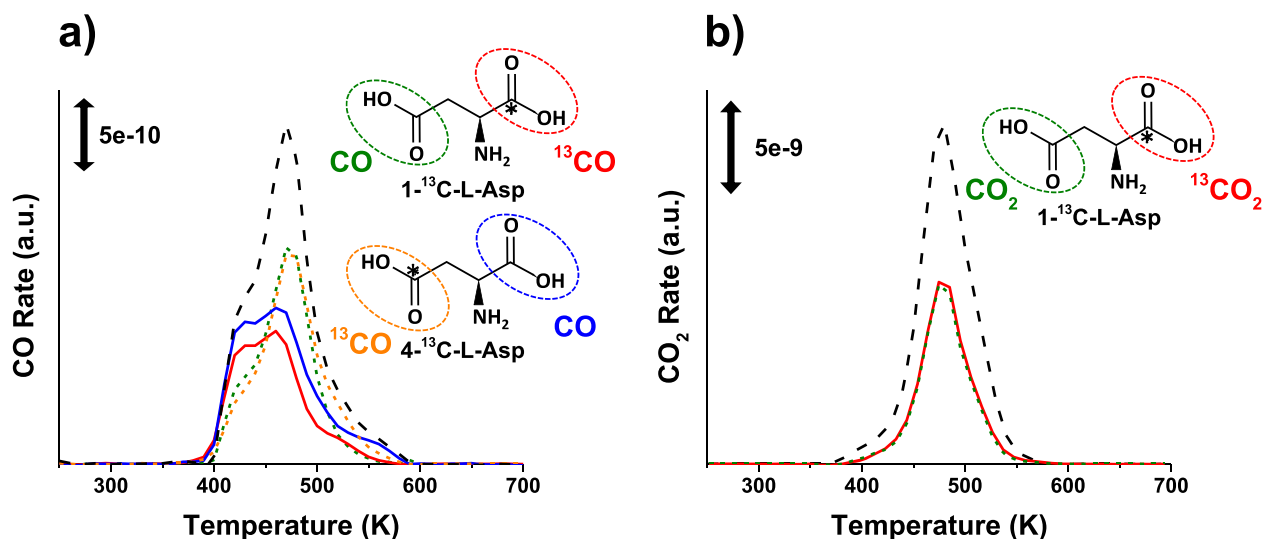


Fig. 5. TPRS spectra of a) CO and b) CO₂ generated during the decomposition of L-Asp, 1-¹³C-L-Asp, and 4-¹³C-L-Asp at monolayer coverage. The asterisks on the molecular structures indicate the positions of the ¹³C isotope label. The dashed black curves correspond to CO and CO₂ arising from the decomposition of unlabeled L-Asp. The solid red curves arise from ¹³CO and ¹³CO₂ originating from the 1-C carbon of 1-¹³C-L-Asp. The dashed green curves arise from ¹²CO and ¹²CO₂ originating from the 4-C carbon of 1-¹³C-L-Asp. The solid blue curve arises from ¹²CO originating from the 1-C carbon of 4-¹³C-L-Asp. Finally, the dashed orange curve arises from ¹³CO originating from the 4-C carbon of 4-¹³C-L-Asp. CO₂ TPRS peaks from 4 to ¹³C-L-Asp were omitted from Fig. 5b for clarity because they were identical to the CO₂ and ¹³CO₂ TPRS curves shown for 1-¹³C-L-Asp decomposition.

coverage relative to that at low coverage. The desorption peak is at $T_p = 481$ K, significantly higher than the peak desorption temperature of $T_p = 427$ K observed at low coverage. Fig. 5b also shows the CO_2 (dashed green) and $^{13}\text{CO}_2$ (solid red) TPRS spectra obtained from decomposition of 1- ^{13}C -L-Asp. The CO_2 and $^{13}\text{CO}_2$ spectra for 4- ^{13}C -L-Asp were omitted because they are indistinguishable from those for 1- ^{13}C -L-Asp. The key features of these spectra are that they reveal identical desorption kinetics for CO_2 and $^{13}\text{CO}_2$, in contrast to the low coverage spectra (Fig. 2b, solid red and dashed green curves) that reveal a distinct difference in the kinetics of CO_2 and $^{13}\text{CO}_2$ production from the two ends of 1- ^{13}C -L-Asp. In addition, there is a coverage dependent shift in the peak desorption temperature from $T_p = 427$ K to 481 K and the decarboxylation kinetics are identical from both ends of the L-Asp molecule. These observations suggest that, at high coverage, the Asp decomposition kinetics are governed by a vacancy-mediated explosion mechanism and that decarboxylation at either end of the molecule is rate limited by some common process. This type of explosion mechanism has been observed and studied quite thoroughly for Asp and tartaric acid on Cu surfaces [25,28,40,41]

At low L-Asp coverage, the 2-C and 3-C carbon atoms were observed desorbing from the Ni(100) surface at 600 K in the form of CO generated by recombination of atomic C and O left on the surface by complete fragmentation of L-Asp. At monolayer coverage of L-Asp there is no desorption of CO at 600 K (Fig. 5a). Instead, the 2-C and 3-C carbon atoms desorb in the form of acetonitrile ($\text{CH}_3\text{C}\equiv\text{N}$, Fig. 6a solid black curve) and hydrogen cyanide ($\text{HC}\equiv\text{N}$, Fig. 6a, solid red curve). Acetonitrile has also been observed as a desorbing product of Asp decomposition on Cu surfaces [28,30,31]. During the thermal decomposition of monolayer L-Asp on Ni(100), $\text{CH}_3\text{C}\equiv\text{N}$ desorbs at $T_p = 481$ K, identical in temperature to the peak CO_2 desorption temperature (Fig. 5b, dashed black curve). In TPRS experiments, $\text{CH}_3\text{C}\equiv\text{N}$ is identified by its mass spectrometer signals at $m/z = (41, 40, 39, 38)$. We have measured independently the fragmentation pattern of $\text{CH}_3\text{C}\equiv\text{N}$ at these four m/z ratios and compared that to the signals observed at these m/z ratios during L-Asp decomposition on Ni(100) (SI Section 2, Fig. S2). This provides strong evidence of the formation of $\text{CH}_3\text{C}\equiv\text{N}$ during Asp decomposition on Ni(100). Furthermore, identical acetonitrile signals are observed at $m/z = 41$ amu during decomposition of L-Asp and 1, 4- $^{13}\text{C}_2$ -L-Asp. This demonstrates unequivocally that the two carbon

atoms in $\text{CH}_3\text{C}\equiv\text{N}$ originate from the 2-C and 3-C atoms in L-Asp.

In addition to the appearance of $\text{CH}_3\text{C}\equiv\text{N}$ as a product of L-Asp decomposition on Ni(100) at monolayer coverage, there are signals at $m/z = 26$ and 27 revealing a product desorbing at $T_p = 498$ K (Fig. 6a). Its fragmentation pattern is consistent with that of $\text{HC}\equiv\text{N}$ [42] which has also been observed in studies of amino acid decomposition on other surfaces [43,44]. Fig. 6b shows a bar graph of the relative intensities at $m/z = 26$ and 27 observed at 498 K during decomposition of five isotopomers of L-Asp. For the unlabeled L-Asp these two fragments correspond to $^{12}\text{C}\equiv^{14}\text{N}^+$ and the parent ion $\text{H}^{12}\text{C}\equiv^{14}\text{N}^+$. To confirm the presence of N in the desorbing species ^{15}N -L-Asp was used. The lack of signal at $m/z = 26$ and the low signal at $m/z = 27$ is consistent with $\text{H}^{12}\text{C}\equiv^{15}\text{N}$ desorption. The signals observed during 1,4- $^{13}\text{C}_2$ -L-Asp and 3,4- $^{13}\text{C}_2$ -L-Asp decomposition are consistent with $\text{H}^{12}\text{C}\equiv^{14}\text{N}$. In other words, the 1-C, 3-C or 4-C atoms do not appear in the $\text{HC}\equiv\text{N}$ product. Finally, the decomposition of 1-4- $^{13}\text{C}_4$ - ^{15}N -L-Asp yields no signals at $m/z = 26$ and 27, consistent with the desorption of $\text{H}^{13}\text{C}\equiv^{15}\text{N}$. In other words, the $\text{HC}\equiv\text{N}$ formed during L-Asp decomposition on Ni(100) at high coverage contains the 2-C carbon atom, exclusively.

In order to study the origin of hydrogen atoms appearing in molecular hydrogen and in water desorption during decomposition of L-Asp at monolayer coverage on Ni(100), we have used D_7 -L-Asp. This allows us to differentiate between D atoms originating in the adsorbed L-Asp and H atoms that adsorb from the background of the UHV chamber during surface preparation and L-Asp adsorption. The appearance of H_2 and HD in Fig. 7a and H_2O and HDO in Fig. 7b demonstrate the presence of some H atoms on the Ni(100) surface due to adsorption from the background. The desorption of H_2 only at 343 K is associated with H atom recombination on the surface. The appearance of H atoms desorbing at higher temperature is associated with H atoms that have exchanged with D atoms in the adsorbed Asp appear from the dehydrogenation and dehydration processes. The XPS spectra of the adsorbed monolayer indicate the presence of both $-\text{NH}(\text{D})_3^+$ groups and $-\text{CO}_2\text{H}(\text{D})$ groups, either of which could be reservoirs of H atoms in adsorbed D_7 -L-Asp.

The primary difference between the TPRS spectra for water and hydrogen during D_7 -L-Asp decomposition at low and monolayer coverages is the appearance of high temperature desorption features at $T_p \approx 480$ K, coinciding with the desorption of CO, CO_2 , and $\text{CH}_3\text{C}\equiv\text{N}$. The molecular hydrogen desorption (Fig. 7a) is dominated by D_2 , suggesting

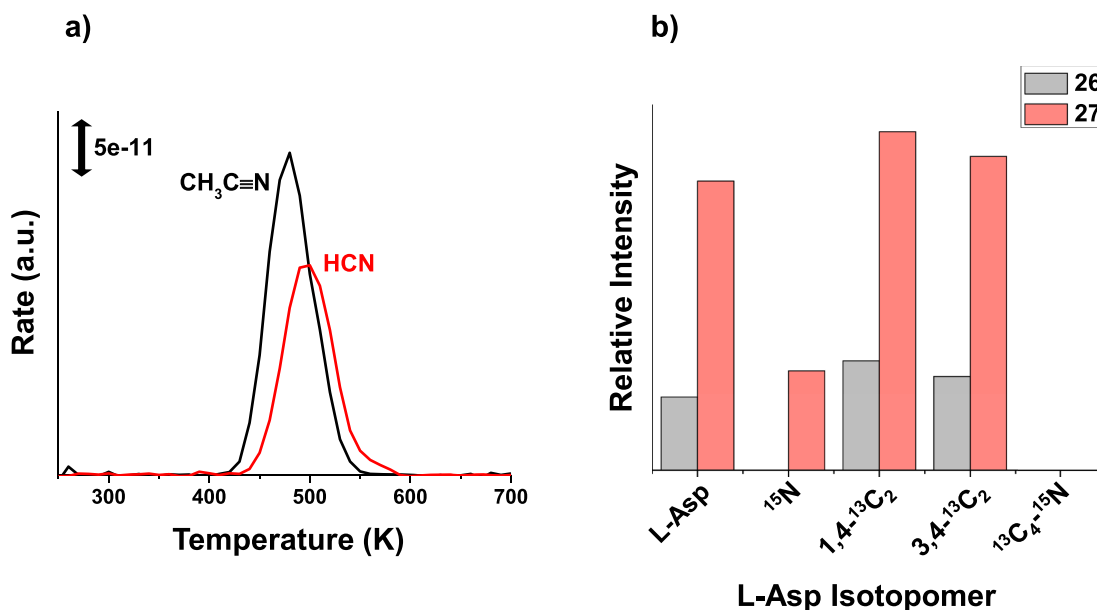


Fig. 6. (a) L-Asp/Ni(100) TPRS spectra at monolayer coverage showing the desorption of $\text{CH}_3\text{C}\equiv\text{N}$ ($m/z = 41$, black) and $\text{HC}\equiv\text{N}$ ($m/z = 27$, red). (b) Relative TPRS signals for $\text{HC}\equiv\text{N}$ at $m/z = 26$ and 27 measured for five different L-Asp isotopomers at monolayer coverage: L-Asp, ^{15}N -L-Asp, 1,4- $^{13}\text{C}_2$ -L-Asp, 3,4- $^{13}\text{C}_2$ -L-Asp, and 1,2,3,4- $^{13}\text{C}_4$ -L-Asp.

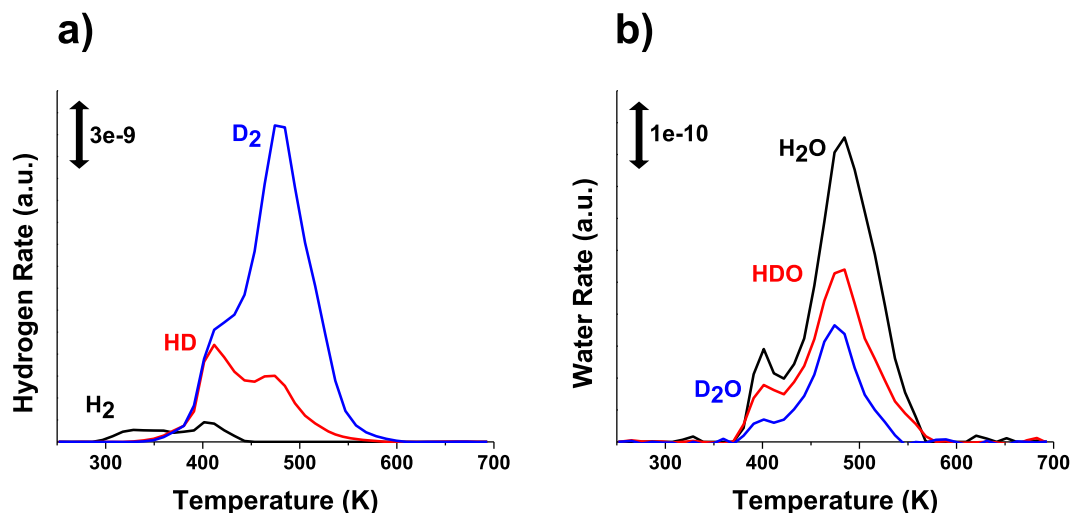


Fig. 7. TPRS spectra of a) H_2 , HD, D_2 and b) H_2O , HDO, D_2O during decomposition of a D_7 -L-Asp monolayer on Ni(100). Three peaks appear at $T_p = 343, 412$ and 481 K in the hydrogen spectra. In the water spectra, two peaks appear at $T_p = 401$ and 486 K.

that it comes from hydrogenolysis of the 2-C and 3-C atoms in the interior of the adsorbed D_7 -L-Asp species. In contrast, the water desorption (Fig. 7b) is dominated by H_2O , suggesting that it may be arising from amine and carboxyl groups that have undergone H-D exchange with surface hydrogen atoms. Alternatively, it is possible that before entering the ionizer of the mass spectrometer desorbing D_2O exchanges D-for H-atoms on the chamber walls.

In summary, isotopic labeling experiments have provided significant insight into the fate of each of the atoms originating in adsorbed L-Asp as it decomposes thermally on Ni(100). It is clear that the products and their yields observed desorbing from the surface differ significantly between low and monolayer L-Asp coverages.

4. Discussion

4.1. Regiospecific origins of L-Asp/Ni(100) decomposition products

Isotope labeling experiments have provided significant insight into the fate of each of the atoms originating in adsorbed L-Asp as it decomposes thermally on Ni(100). It is clear that the products and their yields observed desorbing from the surface differ significantly between low Asp coverage and monolayer coverage. The key findings are summarized in Table 1. CO_2 originates from decarboxylation of the L-Asp and immediate CO_2 desorption with kinetics that are rate limited by the C— CO_2 bond cleavage step. At low L-Asp coverage, the 1C-2C bond breaks (Fig. 2b, solid red and blue curves) prior to the 3C-4C bond (Fig. 2b, dashed green and orange curves). At high coverage, the two bonds break concurrently (Fig. 5b, solid red and dashed green curves) suggesting that the cleavage of one bond triggers the cleavage of the other; i.e. the barrier to breaking the second C— CO_2 bond is lower than the barrier to breaking the first C— CO_2 bond. The CO product desorbing at low temperature (< 550 K, Fig. 2a) originates from the terminal carboxyl groups that we postulate have undergone condensation/

dehydration to yield acyl groups ($\text{R-C}=\text{O}$). Condensation can occur by reaction between $-\text{CO}_2\text{H}$ and $-\text{NH}_2$ groups resulting in the production of H_2O and the formation of an acyl group [45,46]. The CO desorbing at low coverage and high temperature (> 550 K, Figs. 2a and 3) contains carbon atoms originating from the 2-C and 3-C positions only. These are present on the surface as atomic carbon species and react with atomic oxygen present on the Ni(100) surface. That oxygen may have been deposited onto the Ni(100) surface in the course of condensation reactions. Finally, $\text{CH}_3\text{C}\equiv\text{N}$ and $\text{HC}\equiv\text{N}$ (Fig. 6) originate from the 2-C and 3-C positions and are only observed at high coverages. Decarboxylation of L-Asp results in the formation of a $\text{C}_2\text{H}_5\text{N}$ species derived from the 2-C and 3-C carbon atoms. At low coverages this species can decompose completely, but decomposition is blocked at high coverages leading to the appearance of $\text{CH}_3\text{C}\equiv\text{N}$ and $\text{HC}\equiv\text{N}$. At monolayer coverage, $\text{CH}_3\text{C}\equiv\text{N}$ desorption is observed at exactly the same temperature, $T_p = 480$ K (Fig. 6a), as CO_2 desorption (Fig. 5b) suggesting that $\text{CH}_3\text{C}\equiv\text{N}$ appearance is initially triggered by the first C— CO_2 bond cleavage. $\text{HC}\equiv\text{N}$ desorption is observed at a slightly higher temperature, $T_p = 497$ K (Fig. 6a), than $\text{CH}_3\text{C}\equiv\text{N}$ desorption. The $\text{CH}_3\text{C}\equiv\text{N}$ can arise from dehydrogenation of the $\text{C}_2\text{H}_5\text{N}$ species left by decarboxylation of the Asp [30], whereas, $\text{HC}\equiv\text{N}$ requires additional cleavage of the C2-C3 bond.

4.2. Kinetics of Asp decomposition on Ni(100)

The mechanism of L-Asp decomposition on the Ni(100) surface occurs via a complex set of steps with kinetics and selectivities that are clearly dependent on the initial coverage of L-Asp on the surface. Fig. 8 shows the CO and CO_2 TPRS spectra obtained following adsorption of L-Asp on Ni(100) using exposures varying from 3 to 30 min. This reveals the transition from a process at low coverage that yields CO predominantly to a process at high coverage that yields CO_2 predominantly. It also reveals that the formation of CO by atomistic recombination of C and O atoms at $T > 550$ K only occurs at low L-Asp coverages.

The CO_2 TPRS spectra in Fig. 8b are much simpler than those of CO in Fig. 8a and provide some insight into the kinetics of the L-Asp decomposition process. The CO_2 desorption feature appears as a peak at 427 K at low coverage and shifts to 481 K at monolayer coverage. This is accompanied by an undercutting of the low coverage peaks by the high coverage peaks, indicating a decrease in the initial desorption rate with increasing L-Asp coverage. These kinetics are similar to the vacancy-mediated surface explosion kinetics observed for Asp decomposition on Cu surfaces [28,30] although on Ni(100) they are not accompanied by the significant peak narrowing observed on Cu. The vacancy mediated explosion kinetics require the formation of a vacancy in the

Table 1
Origin of C atoms in products derived from L-Asp decomposition on Ni(100).

Product	$\theta_{\text{Asp}} = 0.15$				$\theta_{\text{Asp}} = 1$			
	1-C	2-C	3-C	4-C	1-C	2-C	3-C	4-C
CO_2	✓			✓	✓			✓
$\text{CO}_{<550\text{K}}$	✓			✓	✓			✓
$\text{CO}_{>550\text{K}}$		✓	✓					
$\text{CH}_3\text{C}\equiv\text{N}$						✓	✓	
$\text{HC}\equiv\text{N}$						✓		

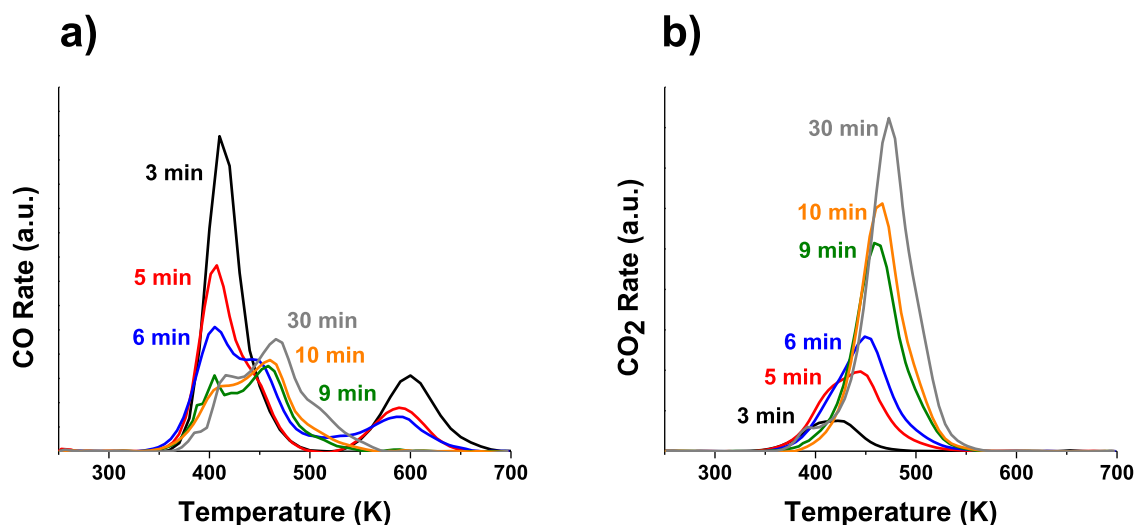


Fig. 8. TPRS of unlabeled L-Asp showing the decomposition products a) CO and b) CO₂ at exposure times: 3, 5, 6, 9, 10, and 30 min (monolayer).

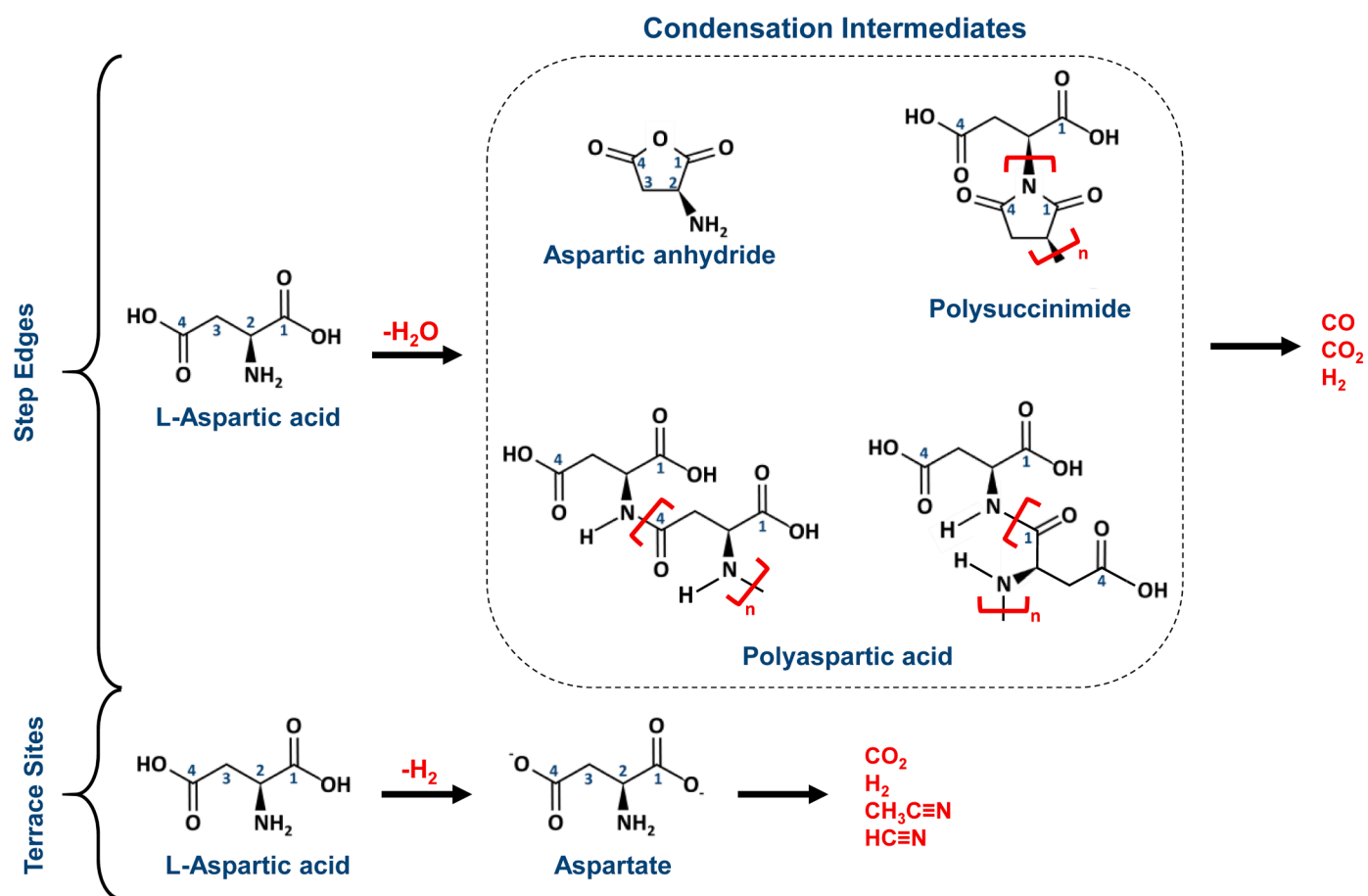


Fig. 9. Reaction scheme and intermediates formed during the thermal decomposition of L-Asp on Ni(100). At low coverage, the mechanism involves the formation of aspartic anhydride, polysuccinimide, and/or polyaspartic acid due to condensation/dehydration of L-Asp occurring along the step edge sites. These intermediates decompose to produce CO, CO₂, and H₂. At higher coverages, L-Asp adsorbs on the terrace sites as aspartate which decomposes to produce CO₂, H₂, CH₃C≡N, and some HC≡N.

adsorbed layer adjacent to an L-Asp in order to initiate its decomposition. Once initiated, subsequent decomposition steps occur concurrently, hence the simultaneous desorption of CO₂ from both ends of the Asp (Fig. 5b) and CH₃C≡N from the interior (Fig. 6a).

4.3. Mechanism of Asp decomposition on Ni(100)

The decomposition mechanism of L-Asp on Ni(100) yields different products and product yields at high and low coverages. At low L-Asp coverages, CO is the predominant product whereas at high L-Asp coverages, CO₂ is dominant and CH₃C≡N production is also observed. The

CO₂ comes directly from decarboxylation of the adsorbed L-Asp. CO also comes from the 1-C and 4-C carboxyl groups of the original L-Asp, but via a more complex path that must include cleavage of a 1C—OH or 4C—OH bond by condensation/dehydration to yield acyl groups that ultimately lead to CO desorption. Prior studies of Asp on Ni(111) [29] and on Pd(111) [26] have suggested that the initial steps of decomposition are condensation/dehydration reactions resulting in the formation of polysuccinimide (Fig. 9) and the elimination of two H₂O molecules per L-Asp. Decomposition of succinimide is likely to yield CO

desorption. Low coverage STM images of Ni(111) reveal the formation of adsorbed species proposed to be polysuccinimide at the step edges on these surfaces [29]. Although the existing study of Asp on Ni(100) [27] excludes the formation of polysuccinimide from polycondensation, that data was collected at higher Asp coverages where the predominant product from Asp decomposition is CO₂. Our varying coverage TPRS data from Fig. 8 shows the clear formation CO product at much lower exposure conditions than in Ref. [27], supporting the formation of the condensation intermediates presented in Figs. 9 and 10. Decomposition

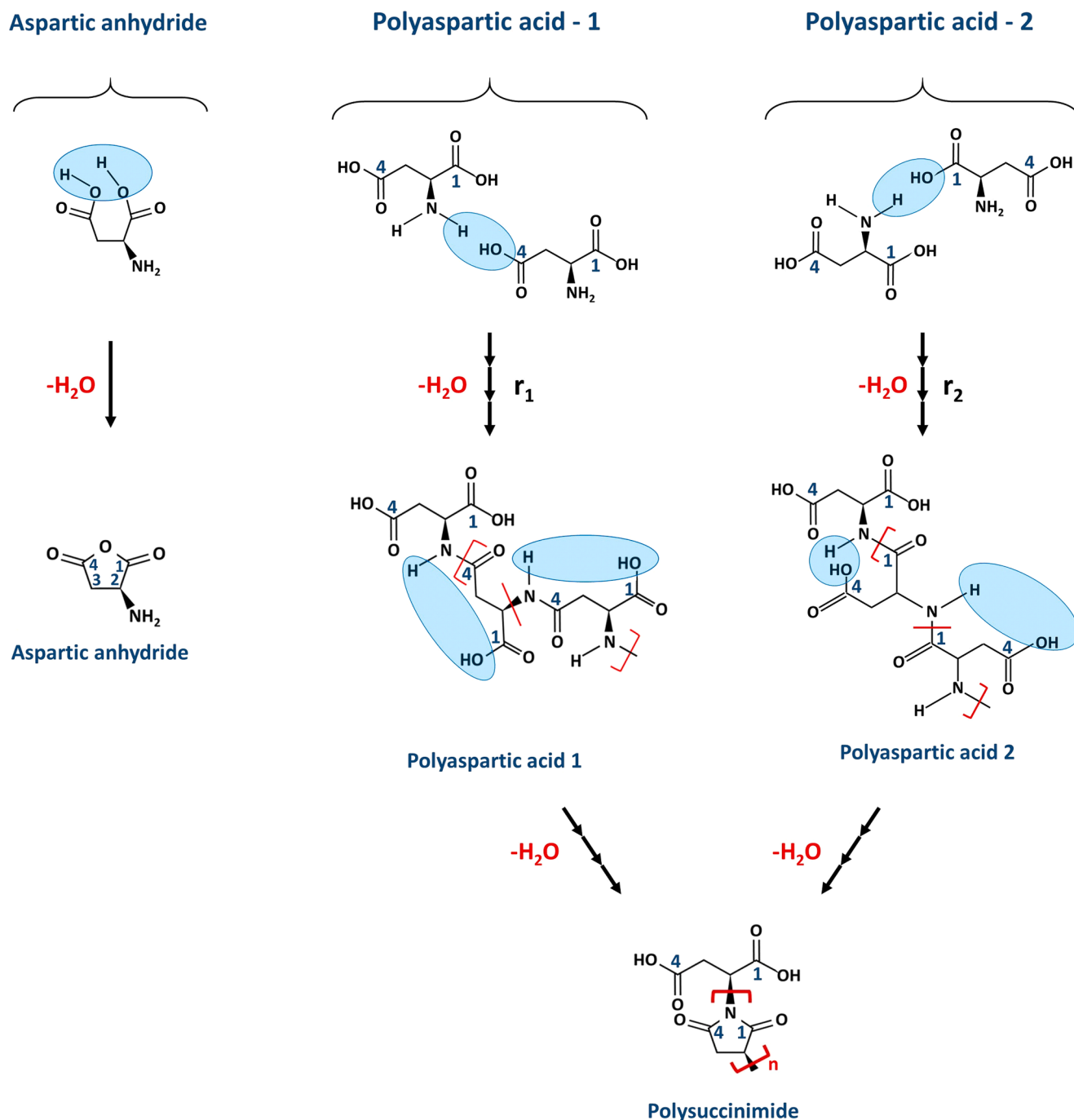


Fig. 10. Formation mechanisms yielding the three polycondensation intermediates shown in Fig. 9. The formation of aspartic anhydride occurs through the intramolecular dehydrocyclization of Asp via reaction between both terminal -OH groups. The blue ellipses highlight the NH and OH pair undergoing dehydration. PolyAsp-1 arises from intermolecular dehydration via sequential reaction of an amine hydrogen with the 4C—OH group to yield N-4C bonds. PolyAsp-2 arises from intermolecular dehydration via sequential reaction of an amine hydrogen with the 1C—OH group to yield N-1C bonds. Polysuccinimide formation from polyAsp-1 occurs via intraAsp dehydration to form N-1C bonds. Similarly, polysuccinimide formation from polyAsp-2 occurs via intraAsp dehydration to form N-4C bonds. In reality, it is likely that the polyAsp contains a mixture of N-1C and N-4C linkages.

of polysuccinimide is likely to yield two CO molecules with equal contributions from the 1-C and 4-C atoms and none from the 2-C and 3-C atoms, consistent with our observations based on isotopic labeling. What is inconsistent with our observations is the observed desorption of CO₂ and the fact that the yields of CO₂ containing 1-C and 4-C atoms are not equal (Fig. 2b). The fact that CO desorption is accompanied by CO₂ desorption at low coverages indicates that not all carboxyl groups have undergone dehydration.

The results above suggest there are other condensation reactions that may be occurring in addition to the formation of polysuccinimide. Studies of Asp pyrolysis in nitrogen [33] have suggested the formation of aspartic anhydride (Fig. 9) via intramolecular dehydration and elimination of one H₂O molecule (Fig. 10). Alternatively, polymerization via intermolecular dehydration can form polyaspartic acid followed by polysuccinimide formation at elevated temperatures [33,47]. Both aspartic anhydride and polysuccinimide have the requisite stoichiometry and connectivity to lead to CO and CO₂ containing equimolar contributions from 1-C and 4-C carboxyl groups. On the other hand, condensation reactions between the -NH₂ group of one molecule and either the 1-C or 4-C carboxyl group of another molecule (Figs. 9 and 10) would probably not have the same probability of occurrence simply because of the asymmetry of L-Asp. Thus, the two amide linkages, N-1C and N-4C, depicted in Fig. 9 would lead to unequal numbers of 1-C or 4-C carboxyl groups, consistent with the asymmetry in 1-CO₂ and 4-CO₂ yields observed in Fig. 2b. If the polyAsp consisted only of N-1C amide linkages (polyAsp 1 in Fig. 10), then the desorbing CO would contain only 1-C atoms and the CO₂ would contain only 1-C atoms. Alternatively, polyAsp 2 which contains only N-4C amide linkages would be expected to yield CO containing only 4-C atoms and CO₂ containing only 1-C atoms. The fact that we observe (Fig. 2) a slight excess of 1-CO₂ and a slight deficit of 1-CO suggests that the dehydrated species on the surface at low coverages has an excess of N-4C over N-1C linkages. These details aside, suffice it to say that, there are several condensation processes that can occur at low coverages and lead to surface species that would be likely to yield both CO and CO₂ during decomposition.

Prior STM studies of Asp on Ni(111) [29] reveal that at low coverage, L-Asp agglomerates at step edges on the surface. These agglomerates could be any one or more of the condensation intermediates shown in Fig. 9. Assuming this also occurs on Ni(100), it is not surprising that the decomposition mechanisms at low and high coverage should be substantially different. In addition to yielding CO coming indirectly from the carboxyl groups, the low coverage mechanism results in the deposition of some O and C atoms on the surface that recombine at high temperatures to yield additional CO (Figs. 2a and 3) arising from the 2-C and 3-C atoms.

At monolayer coverage, when the Asp is adsorbed on the Ni(100) terraces, its decomposition products and kinetics are quite similar to those observed on Cu surfaces [28,30]. The N1s and O1s XPS spectra are consistent with a species that is partially deprotonated at its carboxyl groups and with some of the amine group remaining protonated. The CO₂ produced arises directly from the cleavage of the terminal 1C-2C and 3C-4C bonds to liberate the carboxyl groups. The CO presumably arises from partially dehydrated Asp derived species at the step edges. Finally, the CH₃C≡N is derived from the 2-C and 3-C atoms and the H—C≡N comes solely from the 2-C atoms.

The Asp decomposition pathway on Ni is more complex than on Cu. This is also observed in simulations of related reactions such as the decomposition of formic acid (HCO₂H) on Cu(100) [48] and Ni(100) [49]. On the Cu surface [48], the decomposition of formic acid to CO₂ and H₂ proceeds through the formation of formate and surface hydrogen intermediates only. However on Ni [49], the authors modeled formic acid decomposition kinetics using a number of elementary reactions steps that include the formation of the surface intermediates such as formic anhydride, HCOO, COOH, HCO, and H. A DFT study examining the adsorption and dissociation of water on Cu/Ni bimetallic alloy surfaces found the clean Ni surface has a higher surface energy relative to

Cu and likewise found a stronger water adsorption energy on Ni than on Cu or Ni/Cu bimetallic substrates [50]. As a result, the mechanistic complexity of Asp decomposition on Ni in comparison to Cu may stem from the stronger adsorption energy of water on Ni than on Cu. This could enable alternate decomposition pathway such as dehydration that involve the formation of polycondensation intermediates and water.

The adsorption site occupied by an Asp molecule determines what reaction intermediates are formed and their resulting decomposition pathway. Asp molecules adsorbed along the step edge sites (Fig. 9) will form condensation intermediates through inter- and intra- molecular condensation/dehydration reactions. On the other hand, Asp adsorbed on terrace sites bonds to the surface as aspartate and subsequently decomposes to produce CO₂ and CH₃C≡N products. At low coverage conditions, Asp initially populates the step edge sites. At higher coverages, the step edge sites are already populated hence we still observe decomposition products such as CO and H₂O associated with the formation of the condensation intermediates. However, the more prevalent terrace sites now become populated with aspartate species as revealed by the significant growth of CO₂ products (Fig. 8b) and emergence of new desorbing products such as CH₃C≡N.

5. Conclusions

The thermal decomposition of Asp on Ni(100) follows a complex reaction pathway where at low coverage the dominant pathway involves intra- and inter-molecular condensation/dehydration intermediates such as succinic anhydride, polyaspartic acid, and/or polysuccinimide. The dehydration reactions result in the formation and desorption of H₂O. The remaining intermediates decompose to produce CO, CO₂, and H₂. At higher coverage, the dominant pathway involves the formation of aspartate species that decompose to form CO₂, H₂, CH₃C≡N, and some HC≡N. The use of isotopically labeled isotopomers of Asp has allowed identification of the regiospecific origins of the observed decomposition products and kinetic sequence of their desorption.

Declaration of Competing Interest

The authors declare that they have no known competing financial interests or personal relationships that could have appeared to influence the work reported in this paper.

Acknowledgments

This work was conducted with financial support from the Kaufman Foundation via Grant No. KA2019-105546.

Supplementary materials

Supplementary material associated with this article can be found, in the online version, at doi:10.1016/j.susc.2021.121980.

References

- [1] N. Vargesson, Review thalidomide-induced teratogenesis: history and mechanisms, *Birth Defects Res.* 105 (2015) 140–156 (Part C).
- [2] K. Stoschitzky, G. Egginger, F. Brunner, B. Obermayer-Pietsch, A. Passath, W. Klein, Racemic (R,S)-propranolol versus half-dosed optically pure (S)-propranolol in humans at steady state: hemodynamic effects, plasma concentrations, and influence on thyroid hormone levels, *Clin. Pharmacol. Ther.* 51 (1991) 445–453.
- [3] L. Nguyen, H. He, C. Pham-Huy, Chiral drugs: an overview, *Int. J. Biomed. Sci.* 2 (2006) 85–100.
- [4] C.F. McFadden, P.S. Cremer, A.J. Gellman, Adsorption of chiral alcohols on "chiral" metal surfaces, *Langmuir* 12 (1996) 2483–2487.
- [5] E. Sipos, A. Tungler, I. Bitter, (S)-Proline based chiral modifiers, *J. Mol. Catal. A Chem.* 198 (2003) 167–173.
- [6] I. Busygin, E. Toukoniitty, R. Sillanpaa, D. Murzin, R. Leino, Synthesis of chiral catalysts modifiers by hydrosilylation of cinchonidine and their application in the hydrogenation of 1-phenylpropane-1,2-dione and ethyl pyruvate on a supported pt/al₂o₃ catalyst, *Eur. J. Org. Chem.* (2005) 2811–2821.

- [7] K.E. Simons, G. Wang, T. Heinz, T. Giger, T. Mallat, A. Pfaltz, A. Baiker, A new class of chiral modifiers for the enantioselective hydrogenation of alpha-ketoesters with Pt/Al₂O₃, *Tetrahedron Asymmetry* 6 (1995) 505–518.
- [8] T. Osawa, K. Yoshino, K. Takimoto, O. Takayasu, T. Harada, Enantio-differentiating hydrogenation of methyl acetoacetate over modified Raney nickel catalysts prepared by two-step modifications, *Catal. Lett.* 112 (2006) 167–171.
- [9] V. Humblot, S. Haw, C. Muryrn, W. Hofer, R. Raval, From local adsorption stresses to chiral surfaces (R,R)-tartaric acid on Ni(110), *J. Amer. Chem. Soc.* 124 (2001) 503–510.
- [10] A. Hoek, W.M.H. Sachtler, Enantioselectivity of nickel catalysts modified with tartaric acid or nickel tartrate complexes, *J. Catal.* 58 (1979) 276–286.
- [11] Y. Yun, A.J. Gellman, Enantiospecific adsorption of amino acids on naturally chiral Cu(3,1,17)^{R&S} surfaces, *Langmuir* 31 (2015) 6055–6063.
- [12] Y. Yun, A.J. Gellman, Competing forces in chiral surface chemistry: enantiospecificity versus enantiomer aggregation, *J. Phys. Chem. C* 120 (2016) 27285–27295.
- [13] Y. Yun, A.J. Gellman, Enantioselective separation on naturally chiral metal surfaces: d,L-aspartic acid on Cu(3,1,17)^{R&S} surfaces, *Angew. Commun.* 52 (2013) 3394–3397.
- [14] Y. Izumi, Modified Raney nickel (MRNi) catalyst: heterogeneous enantio-differentiating (asymmetric) catalyst, *Adv. Catal.* 32 (1983) 215–271.
- [15] J.L. Margitfalvi, E. Tfirst, Enantioselective hydrogenation of α -keto esters over cinchona- Pt/Al₂O₃ catalyst molecular modelling of the substrate-modifier interaction, *J. Mol. Catal. A Chem.* 139 (1999) 81–95.
- [16] F. Gao, Y. Wang, L. Burkholder, W.T. Tysoe, Enantioselective chemisorption of propylene oxide on a 2-butanol modified Pd(111) surface: the role of hydrogen-bonding interactions, *J. Am. Chem. Soc.* 129 (2007) 15240–15249.
- [17] M. Mahapatra, L. Burkholder, M. Garvey, Y. Bai, D.K. Saldin, W.T. Tysoe, Enhanced hydrogenation activity and diastereomeric interactions of methyl pyruvate co-adsorbed with R-1-(1-naphthyl)ethylamine on Pd(111), *Nat. Commun.* 7 (2016) 1–8.
- [18] W.Y. Cheong, A.J. Gellman, Enantiospecific desorption of R- and S-propylene oxide from D- or L-lysine modified Cu(100) surfaces, *Langmuir* 28 (2012) 15251–15262.
- [19] T.J. Lawton, V. Pushkarev, D. Wei, F.R. Lucci, D.S. Sholl, A.J. Gellman, E.C. H. Sykes, Long range chiral imprinting of Cu(110) by tartaric acid, *J. Phys. Chem. C* 117 (2013) 22290–22297.
- [20] Q. Chen, D.J. Frankel, N.V. Richardson, Chemisorption induced chirality: glycine on Cu(1 1 0), *Surf. Sci.* 497 (2002) 37–46.
- [21] X. Zhao, R.G. Zhao, W.S. Yang, Scanning tunneling microscopy investigation of L-lysine adsorbed on Cu(001), *Langmuir* 16 (2000) 9812–9818.
- [22] W.Y. Cheong, A.J. Gellman, Energetics of chiral imprinting of Cu(100) by lysine, *J. Phys. Chem. C* 115 (2011) 1031–1035.
- [23] D. Costa, L. Savio, C.M. Pradier, Adsorption of amino acids and peptides on metal and oxide surfaces in water environment: a synthetic and prospective review, *J. Phys. Chem. B* 120 (2016) 7039–7052.
- [24] T.E. Jones, C.J. Baddeley, A. RAIRS, STM and TPD study of the Ni{111}/R,R-tartaric acid system: modelling the chiral modification of Ni nanoparticles, *Surf. Sci.* 513 (2002) 453–467.
- [25] B.S. Mhatre, V. Pushkarev, B. Holsclaw, T.J. Lawton, E.C.H. Sykes, A.J. Gellman, A window on surface explosions: tartaric acid on Cu(110), *J. Phys. Chem. C* 117 (2013) 7577–7588.
- [26] M. Mahapatra, J. Praeger, W.T. Tysoe, Adsorption, assembly, and oligomerization of aspartic acid on Pd(111), *J. Phys. Chem. C* 121 (2017) 13239–13248.
- [27] W. Quevedo, J. Ontaneda, A. Large, J.M. Seymour, R.A. Bennet, R. Grau-Crespo, G. Held, The adsorption geometry of aspartic acid on Ni{100}: a combined experimental and theoretical study, *Langmuir* 36 (2020) 9399–9411.
- [28] B.S. Mhatre, S. Dutta, A. Reinicker, B. Karagoz, A.J. Gellman, Exposive enantiospecific decomposition of aspartic acid on Cu surfaces, *Chem. Commun.* 52 (2016) 14125–14128.
- [29] K.E. Wilson, A.G. Trant, C.J. Baddeley, Interaction of the pro-chiral molecule, methylacetoacetate, with (S)-aspartic acid modified by Ni{111}, *J. Phys. Chem. C* 116 (2011) 1092–1098.
- [30] B. Karagoz, A. Reinicker, A.J. Gellman, Kinetic and mechanism of aspartic acid adsorption and its explosive decomposition on Cu(100), *Langmuir* 25 (2019) 2925–2933.
- [31] Y. Yun, P. Kondratyuk, A.J. Gellman, Steady-state catalytic decomposition of aspartic acid on Cu(111), *J. Phys. Chem. C* (2018).
- [32] T. Nakato, A. Kusuno, T. Kakuchi, Synthesis of poly(succinimide) by bulk polycondensation of L-aspartic acid with an acid catalyst, *J. Polym. Sci. Part A Polym. Chem.* 38 (2000) 117–122.
- [33] Y.Q. Meng, T. Munegumi, K. Harada, Thermal analysis of aspartic acid and its polymers, *Asian J. Chem.* 22 (2010) 2738–2744.
- [34] B. Karagoz, M. Payne, A. Reinicker, P. Kondratyuk, A.J. Gellman, A most enantioselective chiral surface: tartaric acid on all surfaces vicinal to Cu(110), *Langmuir* 35 (2019) 16438–16443.
- [35] A. Shavorskiy, T. Eralp, K. Schulte, H. Bluhm, G. Held, Surface chemistry of glycine on Pt{111} in different aqueous environments, *Surf. Sci.* 607 (2013) 10–19.
- [36] R.E.J. Nicklin, A. Cornish, A. Shavorskiy, S. Baldanza, K. Schulte, Z. Liu, R. A. Bennet, G. Held, Surface chemistry of alanine on Ni{111}, *J. Phys. Chem. C* 119 (2015) 26566–26574.
- [37] F. Gao, Z. Li, Y. Wang, L. Burkholder, W.T. Tysoe, Chemistry of Alanine on Pd(1 1 1): temperature-programmed desorption and X-ray photoelectron spectroscopic study, *Surf. Sci.* 601 (2007) 3276–3288.
- [38] A.L. Cabrera, Desorption studies of hydrogen and carbon monoxide from nickel surfaces using thermal desorption spectroscopy, *J. Vac. Sci. Technol.* 8 (1990) 3229–3236.
- [39] I. Alstrup, I. Chorkendorff, S. Ullmann, Interaction of hydrogen with carbidic carbon on Ni(100), *Surf. Sci.* 293 (1993) 133–144.
- [40] A.J. Gellman, K.H. Ernst, Chiral autocatalysis and mirror symmetry breaking, *Catal. Lett.* 148 (2018) 1610–1621.
- [41] P. Kondratyuk, B. Karagoz, Y. Yun, A.J. Gellman, Initiation of vacancy-mediated, surface explosion reactions: tartaric and aspartic acid on Cu Surfaces, *J. Phys. Chem. C* 123 (2019) 18978–18985.
- [42] W.E. Wallace, P.J. Linstrom, W.G. Mallard, Mass spectra, in: NIST Chem. WebBook, NIST Stand. Ref. Database Number, 69, Gaithersburgh, MD, 2021.
- [43] W.R. Johnson, J.C. Kang, Mechanisms of hydrogen cyanide formation from the pyrolysis of amino acids and related compounds, *J. Org. Chem.* 36 (1971) 189–192.
- [44] K. Harada, Formation of amino-acids by thermal decomposition of formamide-oligomerization of hydrocyanide, *Nature* 214 (1967) 479–480.
- [45] A. Leggio, J. Bagalà, E.L. Belsito, A. Comandè, M. Greco, A. Liguori, Formation of amides: one-pot condensation of carboxylic acids and amines mediated by TiCl₄, *Chem. Cent. J.* 11 (2017) 1–12.
- [46] J. Mosig, C.H. Gooding, A.P. Wheeler, Kinetic and thermal characterization of the hydrolysis of polysuccinimide, *Ind. Eng. Chem. Res.* 36 (1997) 2163–2170.
- [47] S.S. Choi, J.E. Ko, Dimerization reactions of amino acids by pyrolysis, *J. Anal. Appl. Pyrolysis* 89 (2010) 74–86.
- [48] M. Rafiee, H. Bashiri, Catalytic decomposition of formic acid on Cu(100): optimization and dynamic Monte Carlo simulation, *Catal. Commun.* 137 (2020).
- [49] M. Rafiee, H. Bashiri, Dynamic Monte Carlo simulations of the reaction mechanism of hydrogen production from formic acid on Ni(100), *Appl. Surf. Sci.* 475 (2019) 720–728.
- [50] S. Ghosh, S. Hariharan, A.K. Tiwari, Water adsorption and dissociation on copper/nickel bimetallic surface alloys: effect of surface temperature on reactivity, *J. Phys. Chem. C* 121 (2017) 16351–16365.